



CHORUS

This is the accepted manuscript made available via CHORUS. The article has been published as:

Broadband, Multiband, and Multifunctional All-Dielectric Metasurfaces

Amin Ranjbar and Anthony Grbic

Phys. Rev. Applied **11**, 054066 — Published 23 May 2019

DOI: [10.1103/PhysRevApplied.11.054066](https://doi.org/10.1103/PhysRevApplied.11.054066)

Broadband, multiband, and multifunctional all-dielectric bianisotropic metasurfaces

Amin Ranjbar and Anthony Grbic*

*Department of Electrical Engineering and Computer Science,
University of Michigan,
Ann Arbor, Michigan 48109-2122, USA
(Dated: March 27, 2019)*

All-dielectric, bianisotropic metasurfaces with tailored polarization and spectral responses are studied, and a systematic approach to their design is developed. It is shown that a wide range of polarization transformations over broad bandwidths, as well as multiple bands, can be implemented by cascading subwavelength dielectric gratings. The subwavelength gratings, modeled as anisotropic layers, are cascaded to form metasurfaces that control the polarization of impinging waves. These metasurfaces are a lowloss alternative to their lossy, plasmonic counterparts at optical frequencies, and can replace conventional, bulky optical components. The multifunctional performance and compactness (wavelength-sized thickness) of the proposed devices will also find use at millimeter-wave frequencies. Example metasurfaces are presented and their performance verified through full-wave simulation. This work demonstrates the flexibility with which cascaded subwavelength gratings can realize unprecedented polarization conversion/control with varied spectral responses.

I. INTRODUCTION

The manipulation of an electromagnetic waves' polarization state has broad applicability in areas such as polarimetric imaging, biosensing, and optical communication [1–3]. At microwave and millimeter-wave frequencies, polarization control can be achieved with cascaded patterned metallic claddings. Through subwavelength texturing, one can achieve a wide range of electric sheet admittances, which can then be cascaded to realize tailored electric, magnetic, and magneto-electric surface properties [4]. These responses can be used to refract a wavefront, focus it, as well as control its polarization [4–8].

In optical and quasi-optical systems, polarization converters are implemented by cascading wave plates and polarizers. Wave plate retarders use birefringent crystals and require a significant propagation distance to establish the required phase differences between orthogonal polarizations. In addition, to mitigate their narrowband performance, multilayered films are employed, yielding bulky structures incompatible with nano-integration.

The advent of metasurfaces has led to the realization of low-profile devices with unprecedented functionalities that are not achievable using naturally birefringent media. Advances in nano-fabrication have also led to the emergence of new class of metasurfaces composed of all-dielectric meta-atoms [10–13]. These structures can trace their roots to dielectric resonator antennas which have a rich history in the microwave community, dating back to the 1980s [14, 15]. More recently, arrays of dielectric resonators have been used to devise all-dielectric transmissive and reflective nano-antennas at optical wavelengths [16–19].

Huygens sources realized from silicon nano-cylinders have been used to mold wavefronts in a reflectionless

manner across ultrathin distances [20–22]. Full transmission and phase coverage is achieved by overlapping electric and magnetic Mie resonances of silicon nano-cylinders. An alternative approach to realizing a transmissive metasurface, that provides spatially-varying control of phase and polarization, with efficiency exceeding 80% is reported in Refs. [23, 24]. These all-dielectric metalenses are implemented using elliptical silicon posts and nanofins with various dimensions and orientations that impose desired polarization-dependent phase gradients. Perfect mirrors have also been implemented by exciting the magnetic Mie resonances of nano-resonators [25, 26]. Mie-resonant nano-particles have been employed in realizing anti-reflection coatings across the visible spectrum [27]. In addition, broadband linear polarization conversion and vortex beam generation with high efficiency have also been reported using meta-reflectarray nano-structures [28].

Strong chirality has been shown using cascaded silicon crosses, tensor Huygens resonators, and nanogratings [29–31]. Transparent dielectric meta-atoms with magneto-electric and Fano resonances, have been demonstrated by exploiting the coupling between dielectric resonators [32–35]. In [36], electromagnetic induced transparency was demonstrated using Fano-resonant all-dielectric structures. Planar chirality was used to realize ultrathin circular polarizers with dielectric metasurfaces in [37]. In addition, cylindrical dielectric particles with broken symmetries have revealed bianisotropic properties, by exploiting losses within the dielectrics [38]. These earlier bianisotropic structures are design specific and their generalization to other forms of polarization control is not straightforward. All-dielectric metasurfaces reported to date have shown a limited range of bianisotropic properties due to the scatterers and single-layer topologies used that provide limited degrees of freedom.

High contrast gratings can be thought of as the direct predecessor of dielectric metasurfaces. The fabrication process for dielectric gratings is well established,

* agrbic@umich.edu

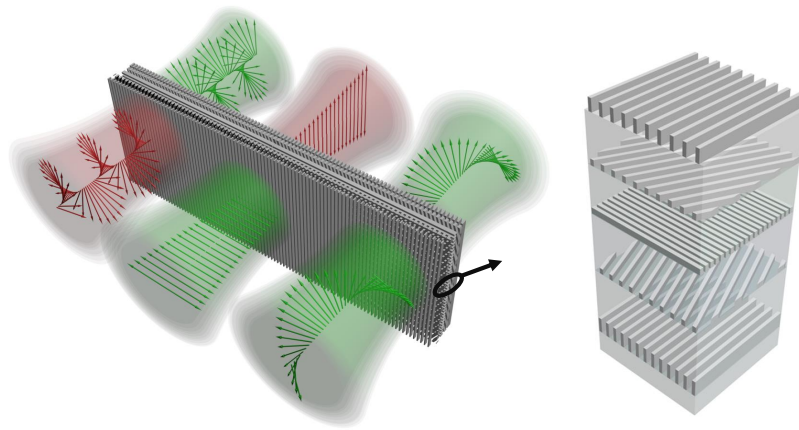


FIG. 1: An exploded view of a generic, all-dielectric metasurface composed of a stack of subwavelength dielectric gratings with varying axes orientations separated by dielectric spacers. The multilayer metasurface can control the polarization of the impinging waves in a multiband, multifunctional manner.

and has led to a variety of devices such as broadband and anomalous reflectors [39–41], achromatic lenses [42, 43], flat lenses [44, 45], filters [46, 47], diffractive optical components [48], wave-plates [49–51], and linear and circular polarizers [60–62]. Binary-phase gratings and blazed gratings have been utilized in diffractive and refractive optical components and deep-subwavelength, high-contrast gratings used to form birefringence [51, 63].

Complex, multilayered/stacked gratings are found in the natural environment, providing polarization filtering and polarimetric vision to living organisms [64–67]. In addition, a wide variety of electromagnetic phenomena have been demonstrated by employing multilayered structures and controlling the physical and electrical properties of each layer [52–59]. In this work, an approach to controlling polarization with multilayer, high-contrast, subwavelength gratings is reported. It is shown that by cascading subwavelength gratings with varying orientations, shown in Fig.1, a variety of bianisotropic properties can be obtained, allowing a wide range of polarization transformations and tailored frequency responses.

The proposed, low-profile metasurfaces can be designed to have broadband, multiband, and multifunctional responses by exploiting the added degrees of freedom (increased dimensionality) offered by multilayered metasurfaces. Broadband metasurfaces realize a given polarization conversion over a large continuous bandwidth. Multiband metasurfaces realize a common polarization conversion over different bands, while multifunctional metasurfaces realize different polarization conversions over different bands [68–77]. It will be shown that multilayer, all-dielectric metasurfaces with these three types of responses can be designed in a systematic manner.

The multilayer, all-dielectric metasurfaces are modeled analytically, and therefore their optimization is rapid, and does not require iterative full wave simulations [4–

8, 29, 30]. The metasurfaces are represented as stratified media, and modeled using the Wave matrix (Transfer matrix) representation of cascaded networks [78–80]. High-contrast, subwavelength gratings are simply modeled as anisotropic dielectric layers. In the long wavelength limit, subwavelength gratings can be homogenized and represented as uniaxial slabs with effective permittivities that can be written in closed form. The effective medium approach is applied to design the metasurfaces for normal excitation. Higher-order Floquet modes are bound to the gratings due to their subwavelength periodicities, and as a result zeroth-order coupling between the gratings only needs to be considered.

Using low-loss dielectrics avoids the ohmic dissipation observed in metallic structures. In addition, high-contrast subwavelength gratings can generate far greater phase accumulation across a given thickness than natural crystals. As a result, their overall thickness is significantly reduced compared to polarization controlling devices consisting of natural birefringent media, conventional cascaded wave-plates, and commercially available devices based on liquid crystals [81]. It will be shown that the performance of these structures is maintained over a wide angular range despite their wavelength-scale thickness.

II. SUBWAVELENGTH GRATINGS

An extensive body of work exists on the electromagnetic properties of periodic structures and diffraction gratings. Gratings have been widely used in optoelectronics, acousto-optics, holography, spectroscopy, and beam shaping [48]. Structured periodic surfaces with periods smaller than the wavelength can exhibit birefringence, which suggests interesting applications in the implementation of polarizers, wave plates, and anti-reflection coatings. Several approaches have been used

to homogenize gratings in the past [82, 83]. Studies have focused on the derivation of closed-form expressions for their effective refractive indices under TE and TM incidence. Expressions for the effective permittivities of 1-D and 2-D gratings have been derived in the quasi-static and non-quasi-static limits [85, 86].

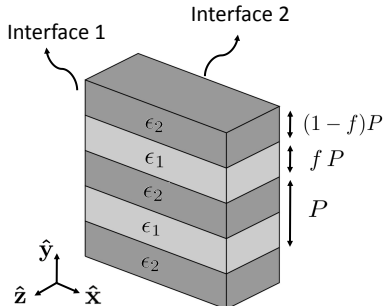


FIG. 2: A subwavelength grating. Under TM (x -polarized) and TE (y -polarized) incidence, it exhibits different effective permittivities, and can be approximated as a uniaxial slab.

Subwavelength gratings are the building block of the proposed multilayer, all-dielectric metasurfaces. In the long wavelength limit, the subwavelength grating, shown in Fig.2, can be approximated as a uniaxial slab with the same physical thickness as the subwavelength grating with effective permittivities given by,

$$\epsilon_x = f\epsilon_1 + (1-f)\epsilon_2, \quad \frac{1}{\epsilon_y} = \frac{f}{\epsilon_1} + \frac{1-f}{\epsilon_2}. \quad (1)$$

Eq.(1) provides expressions for the effective permittivities, ϵ_x and ϵ_y , for a wave propagating perpendicular to the stack with the electric field along \hat{x} (TM polarization) and \hat{y} (TE polarization), respectively. The variable f denotes the filling factor of medium 1. These expressions hold for deep-subwavelength gratings under normal incidence. More accurate expressions for the effective permittivities of gratings were reported in [82–84], which account for larger period to wavelength ratios. Here, subwavelength gratings are used with period to wavelength ratio of,

$$\frac{p}{\lambda} \approx 0.1 \quad (2)$$

The Wave Matrix (WM) representation of cascaded networks will be used to model wave propagation (normal incidence) within the proposed multilayer metasurfaces shown in Fig.1. Since WMs relate the incident to the scattered fields, they are closely related to scattering parameters [78]. Specifically, WMs relate the forward and backward propagating waves in one layer to those in the next layer. As a result, the WM of a cascaded network can be computed by multiplying the WMs of its constituent components [79]. The multilayer metasurface considered consists of stacked subwavelength gratings (Fig.1). A subwavelength grating can be thought

of as a uniaxial slab with two interfaces and two phase delays associated with the two orthogonal polarizations (Fig.2). The WM of interface 1 can be found by applying boundary conditions to the tangential electric and magnetic fields, and solving for the incident and reflected waves in one region in terms of those in the next region,

$$\mathbb{M}_{inter}^{(1)} = \mathbf{t}_x \otimes \begin{pmatrix} 1 & 0 \\ 0 & 0 \end{pmatrix} + \mathbf{t}_y \otimes \begin{pmatrix} 0 & 0 \\ 0 & 1 \end{pmatrix}, \quad (3)$$

where,

$$\mathbf{t}_u = \frac{1}{T_u} \begin{pmatrix} 1 & R_u \\ R_u & 1 \end{pmatrix}, \quad (4)$$

The symbol \otimes represents the Kronecker tensor product. Variables T_u and R_u are the Fresnel transmission and reflection coefficients,

$$R_u = \frac{\eta_u - \eta_o}{\eta_u + \eta_o}, \quad T_u = \frac{2\eta_u}{\eta_u + \eta_o}, \quad (5)$$

where,

$$\eta_u = \frac{\eta_o}{\sqrt{\epsilon_{ru}}}. \quad (6)$$

and η_o is the free space wave impedance. The variable u can be either x or y and ϵ_{ru} is the relative effective permittivity of the grating, given by Eq.(1), for a u -polarized incident wave.

As noted, higher-order Floquet harmonics are confined to the surface of the grating due to the subwavelength periodicity of the gratings. Therefore, it is sufficient to only study the propagation of the zeroth-order harmonics. As a result, the phase progression inside the slab can be written as,

$$\mathbb{M}_{delay} = \Phi_x \otimes \begin{pmatrix} 1 & 0 \\ 0 & 0 \end{pmatrix} + \Phi_y \otimes \begin{pmatrix} 0 & 0 \\ 0 & 1 \end{pmatrix}. \quad (7)$$

where,

$$\Phi_u = \begin{pmatrix} e^{j\varphi_u} & 0 \\ 0 & e^{-j\varphi_u} \end{pmatrix}, \quad (8)$$

and,

$$\varphi_u = \varphi_0 \sqrt{\epsilon_{ru}}, \quad \varphi_0 = k_0 d. \quad (9)$$

The variable φ_0 represents the electrical thickness of the anisotropic slab in terms of free space wavelengths. Variable d is the physical thickness of the slab, and k_0 is the propagation constant in free space.

The total WM of an anisotropic slab is obtained by multiplying the WMs of the constituent elements: interface 1, the phase delay within the slab, and interface 2. Since the WM of interface 2 is the inverse of interface 1 (Fig.2), the total WM will be,

$$\mathbb{M}^{aniso} = \mathbb{M}_{inter}^{(1)} \mathbb{M}_{delay} \mathbb{M}_{inter}^{(2)} =$$

$$(\mathbf{t}_x \Phi_x \mathbf{t}_x^{-1}) \otimes \begin{pmatrix} 1 & 0 \\ 0 & 0 \end{pmatrix} + (\mathbf{t}_y \Phi_y \mathbf{t}_y^{-1}) \otimes \begin{pmatrix} 0 & 0 \\ 0 & 1 \end{pmatrix}. \quad (10)$$

In writing Eq.(3), Eq.(7), and Eq.(10), it is assumed the crystal axes of the grating and the coordinate system are aligned. However, for a rotation angle θ , the WM is transformed as,

$$\mathbb{M}_{rot}^{aniso} = (\mathbf{I} \otimes \mathbf{R}(\theta)) \mathbb{M}^{aniso} (\mathbf{I} \otimes \mathbf{R}^T(\theta)), \quad (11)$$

where \mathbf{I} is the 2×2 identity matrix and \mathbf{R} is the rotation matrix,

$$\mathbf{R}(\theta) = \begin{pmatrix} \cos \theta & -\sin \theta \\ \sin \theta & \cos \theta \end{pmatrix}. \quad (12)$$

The transformation given by Eq.(11) is general and applicable to all network representations including impedances, scattering, and ABCD matrices C[87]. Applying Eq.(11) to the WM of the anisotropic slab, results in,

$$\begin{aligned} \mathbb{M}_{rot}^{aniso} = & (\mathbf{t}_x \Phi_x \mathbf{t}_x^{-1}) \otimes \begin{pmatrix} \cos^2 \theta & \sin \theta \cos \theta \\ \sin \theta \cos \theta & \sin^2 \theta \end{pmatrix} \\ & + (\mathbf{t}_y \Phi_y \mathbf{t}_y^{-1}) \otimes \begin{pmatrix} \sin^2 \theta & -\sin \theta \cos \theta \\ -\sin \theta \cos \theta & \cos^2 \theta \end{pmatrix}. \end{aligned} \quad (13)$$

This WM of an anisotropic slab will be used to model subwavelength gratings, and efficiently design the cascaded metasurface, consisting of stacked subwavelength gratings.

III. CASCADED SUBWAVELENGTH GRATINGS

It has been shown that a wide range of polarization transformations can be realized by cascading anisotropic metallic sheets [4–7]. A systematic design technique was developed for such metasurfaces to obtain targeted scattering performances in [4]. Here, a systematic approach for the design of cascaded dielectric metasurfaces is developed. We can define a general bianisotropic response by stipulating the desired scattering parameters: reflection and transmission coefficients of the co-polar and cross-polar field components. The S-matrix will be a 4×4 matrix, corresponding to a four port network, given that two components of the field exist on either side of the cascaded dielectric metasurface.

The metasurface considered here is a cascade of subwavelength gratings and spacers. The WM of each subwavelength grating is given by Eq.(13). The WM of the isotropic spacers ($\epsilon_s = \epsilon_x = \epsilon_y$) is found by setting,

$$\mathbf{t} = \mathbf{t}_x = \mathbf{t}_y, \quad \Phi = \Phi_x = \Phi_y, \quad (14)$$

in Eq.(13). This results in,

$$\mathbb{M}^{iso} = (\mathbf{t} \Phi \mathbf{t}^{-1}) \otimes \mathbf{I}, \quad (15)$$

The WMs of the constituent elements are multiplied to obtain the total WM of the cascaded metasurface,

$$\mathbb{M}_t = \prod_{i=1}^N (\mathbf{I} \otimes \mathbf{R}(\theta_i)) \mathbb{M}_i^{aniso} (\mathbf{I} \otimes \mathbf{R}^T(\theta_i)) \mathbb{M}_i^{iso}, \quad (16)$$

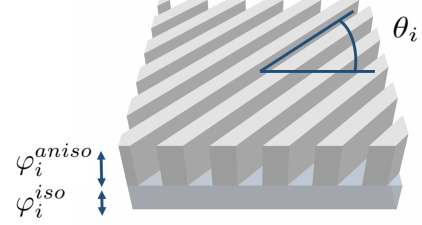


FIG. 3: Design variables that need to be determined in the i 'th layer of cascaded metasurface: grating thickness, filling ratio, rotation angle, and thickness of the isotropic spacer.

This total WM is then converted to its S-matrix representation [78, 79] using,

$$\begin{pmatrix} \mathbf{S}_{11} & \mathbf{S}_{12} \\ \mathbf{S}_{21} & \mathbf{S}_{22} \end{pmatrix} = \begin{pmatrix} \mathbf{0} & \mathbf{M}_{11} \\ -\mathbf{I} & \mathbf{M}_{21} \end{pmatrix}^{-1} \begin{pmatrix} \mathbf{I} & -\mathbf{M}_{12} \\ \mathbf{0} & -\mathbf{M}_{22} \end{pmatrix}. \quad (17)$$

and equated to the desired scattering matrix.

Optimization can then be used to solve for the design parameters ($\varphi_i^{aniso}, \varphi_i^{iso}, \theta_i, f_i$) of the constitutive layers depicted in Fig.3, as well as the number of layers, N . The subwavelength grating, in layer i , rotated by an angle θ_i , has a free space electrical thickness φ_i^{aniso} , and filling ratio f_i . The isotropic spacer has a free space electrical thickness φ_i^{iso} . The isotropic spacers are needed for the optimization process to converge. It should be noted that the evanescent coupling between the gratings is negligible since they are deeply subwavelength. Therefore, there is no minimum thickness for the spacers. Only upper bounds are set for the spacer thicknesses in the optimization process.

Optimization of a transparent metasurface involves minimizing the following cost function,

$$\begin{aligned} |\mathbf{S}_{21} - \mathbf{S}_{21}^d| = & |S_{21}^{xx} - S_{21}^{xxd}| + |S_{21}^{xy} - S_{21}^{xyd}| \\ & + |S_{21}^{yx} - S_{21}^{yxd}| + |S_{21}^{yy} - S_{21}^{yyd}|, \end{aligned} \quad (18)$$

where \mathbf{S}_{21} is given by Eq.(17) and \mathbf{S}_{21}^d is the desired transmission matrix. The component layers are assumed to be reciprocal, and as the result, $\mathbf{S}_{12} = \mathbf{S}_{21}^T$. Since a reflective metasurface is described by reflection matrices, \mathbf{S}_{11}^d and \mathbf{S}_{22}^d , the cost function for a reflective metasurface will be defined as,

$$|\mathbf{S}_{11} - \mathbf{S}_{11}^d| + |\mathbf{S}_{22} - \mathbf{S}_{22}^d|. \quad (19)$$

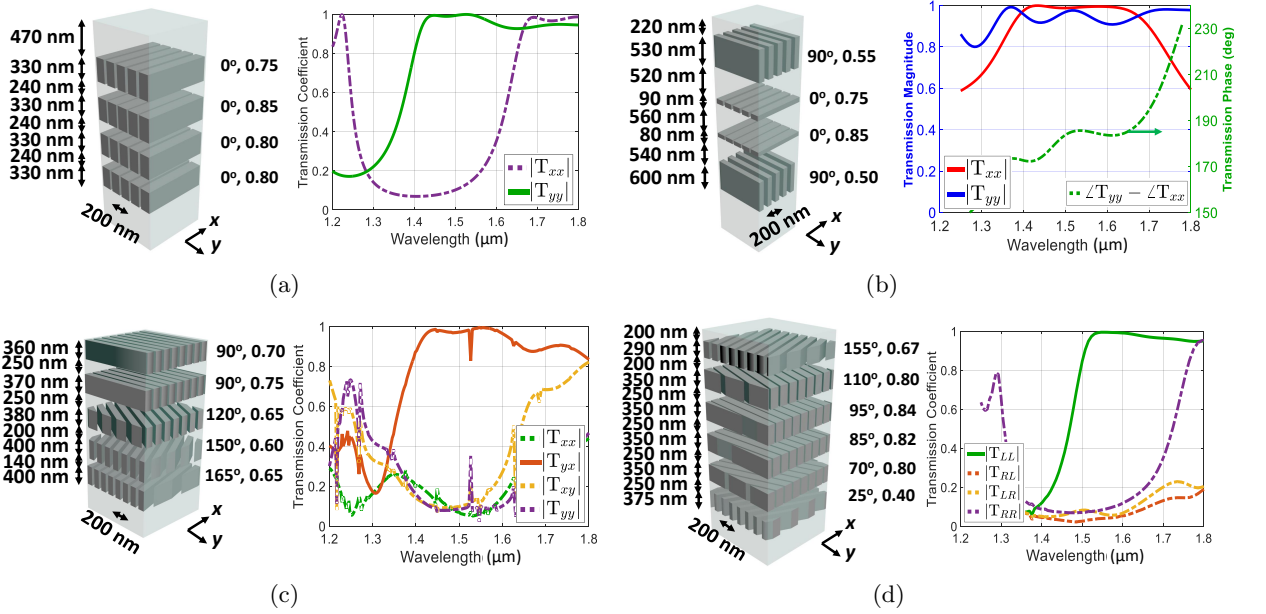


FIG. 4: Cascaded all-dielectric metasurfaces realizing a (a) symmetric linear polarizer, (b) half-wave plate, (c) asymmetric linear polarizer, and (d) symmetric circular polarizer. The thicknesses of the layers are listed to the left side of each structure. The grating filling ratio and rotation angle (with respect to the x -axis) are shown to the right. The grating period is identical in all the layers. T_{yx} denotes the transmission coefficient from a linearly x -polarized wave to a y -polarized wave, and T_{LR} denotes the transmission coefficient from a right-handed to a left-handed circularly polarized wave.

IV. DESIGN PROCESS AND EXAMPLES

The proposed all-dielectric metasurfaces can play a major role at NIR and optical frequencies, where metallic losses significantly degrade the efficiency of plasmonic metasurfaces [9]. In fact, efficiencies approaching 100% can be achieved by exploiting low-loss dielectrics. The design technique and resulting metasurfaces can be employed to realize compact, reciprocal, low-loss and broadband transmissive or reflective optical components such as symmetric and asymmetric, linear and circular polarizers, and waveplates.

To begin, a symmetric linear polarizer will be demonstrated by cascading subwavelength gratings. The Jones matrices of x and y symmetric linear polarizers are,

$$\mathbf{P}_x \equiv e^{j\phi} \begin{pmatrix} 1 & 0 \\ 0 & 0 \end{pmatrix}, \quad \mathbf{P}_y \equiv e^{j\phi} \begin{pmatrix} 0 & 0 \\ 0 & 1 \end{pmatrix}, \quad (20)$$

where the variable ϕ represents the phase delay across the structure. In the following examples, the gratings are assumed to be made of silicon, and the spacers and trenches of silicon dioxide. At a wavelength of $1.5 \mu\text{m}$, the permittivities of silicon and silicon dioxide are,

$$\epsilon_g = 12.1, \quad \epsilon_s = \epsilon_t = 2.1. \quad (21)$$

where ϵ_g , ϵ_s , and ϵ_t are the permittivities of the grating, spacers, and trenches, respectively. The effective anisotropic permittivity of each subwavelength grating

is found using Eq.(1). The WM of each grating layer, \mathbb{M}_{aniso} , is calculated using Eq.(10). The WM of the spacers, \mathbb{M}_{iso} , is given by Eq.(15). The total WM is then computed by multiplying the WMs of the gratings and spacers using Eq.(16). Inserting the total WM into Eq.(17) yields the corresponding S-matrix. The design parameters of the cascaded metasurface are determined numerically by employing the nonlinear programming solver, *fmincon*, in *Matlab*, and minimizing the cost function given by Eq.(18),

$$|\mathbf{S}_{21} - \mathbf{S}_{21}^d| < \epsilon$$

and Eq.(19),

$$|\mathbf{S}_{11} - \mathbf{S}_{11}^d| + |\mathbf{S}_{22} - \mathbf{S}_{22}^d| < \epsilon \quad (22)$$

For transmissive or reflective metasurfaces, respectively. Where ϵ can be arbitrary small (higher convergence) for increasing numbers of layers. The optimization rapidly converges since the effective permittivities of the anisotropic layers are written in closed form (Eq.(1)). The design dimensions of a cascaded dielectric polarizer consisting of 4 layers of subwavelength gratings are shown in Fig.4a for a design wavelength of $1.5 \mu\text{m}$. It should be noted that the reported metasurfaces are optimized assuming that the constitutive materials are dispersionless (Eq.(1)). However, the full-wave simulated performance of the device accounts for the frequency dependence of the dielectric materials and their associated losses.

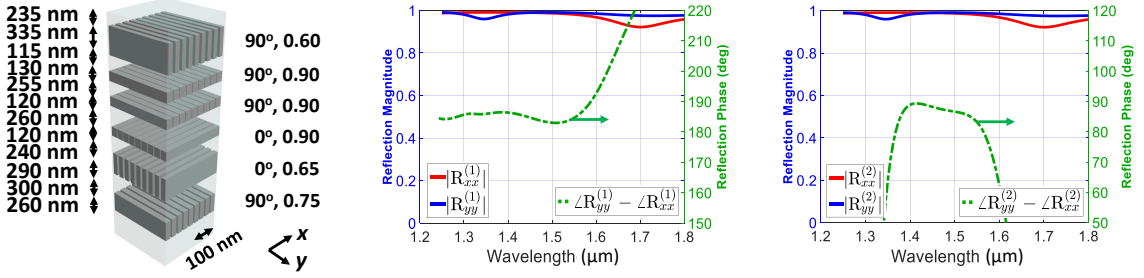


FIG. 5: A reflective metasurface that acts as a half-wave plate from the top side and a reflective quarter-wave plate from the bottom side. The plots show that x and y linearly polarized incident waves are highly reflected ($R_{xx}^{(i)} = R_{yy}^{(i)} \approx 1$) with 180° and 90° phase difference ($\angle R_{yy}^{(i)} - \angle R_{xx}^{(i)} \approx 180^\circ, 90^\circ$) between orthogonal components of reflected fields when excited from each side.

Similarly, cascaded subwavelength gratings can be designed to realize wave-plates. For example, a half-wave plate is typically implemented using naturally birefringent crystals. However, at optical and NIR wavelengths wideband, reflection-less half-wave plates are bulky, and do not lend themselves to nano-integration [88]. The Jones matrix of a half-wave plate is,

$$\mathbf{H} \equiv e^{j\phi} \begin{pmatrix} -1 & 0 \\ 0 & 1 \end{pmatrix}, \quad (23)$$

A half-wave plate is shown in Fig.4b. It is designed in the same way as the polarizer.

A cascade of polarizers and wave-plates are commonly used to control polarization in various ways. For example, an asymmetric linear polarizer can be implemented by cascading a half-wave plate and a rotated (45°) polarizer. In contrast to a symmetric linear polarizer that transmits one linearly polarized incident wave and reflects the other, an asymmetric linear polarizer converts a linear polarization ($\hat{\mathbf{x}}$) to an orthogonal polarization ($\hat{\mathbf{y}}$) upon transmission. On the other hand, it reflects the orthogonal polarization ($\hat{\mathbf{y}}$). The Jones matrices for x and y polarized asymmetric linear polarizers are,

$$\mathbf{AP}_x \equiv e^{j\phi} \begin{pmatrix} 0 & 0 \\ 1 & 0 \end{pmatrix}, \quad \mathbf{AP}_y \equiv e^{j\phi} \begin{pmatrix} 0 & 1 \\ 0 & 0 \end{pmatrix}, \quad (24)$$

A structure, consisting of 5 layers of subwavelength gratings, that realizes an asymmetric linear polarizer is shown in Fig.4c. Note that cascading the half-wave plate of Fig.4b and the polarizer of Fig.4a will also yield a broadband asymmetric linear polarizer. However, with the integrated design, shown in Fig.4c, the same performance can be obtained with a reduced number of layers, and reduced overall thickness.

Analogous to a linear polarizer, a symmetric circular polarizer transmits one handedness of circular polarization and reflects the other. Reflectionless metasurfaces with circular polarization selectivity require electric, magnetic, and magneto-electric surface properties [4]. The Jones matrices for left-handed and right-handed

symmetric circular polarizers are [88],

$$\mathbf{CP}_l \equiv \frac{e^{j\phi}}{2} \begin{pmatrix} 1 & -j \\ j & 1 \end{pmatrix}, \quad \mathbf{CP}_r \equiv \frac{e^{j\phi}}{2} \begin{pmatrix} 1 & j \\ -j & 1 \end{pmatrix}, \quad (25)$$

In contrast to the symmetric circular polarizer, an asymmetric circular polarizer converts one circular polarization to the orthogonal polarization, upon transmission. On the other hand, it reflects the orthogonal polarization. The Jones matrices of left-handed and right-handed asymmetric circular polarizers are [88],

$$\mathbf{ACP}_l \equiv \frac{e^{j\phi}}{2} \begin{pmatrix} 1 & -j \\ -j & -1 \end{pmatrix}, \quad \mathbf{ACP}_r \equiv \frac{e^{j\phi}}{2} \begin{pmatrix} 1 & j \\ j & -1 \end{pmatrix}. \quad (26)$$

A symmetric circular polarizer is conventionally implemented by placing a 45° rotated linear polarizer between two quarter-wave plates with their slow axes aligned, while an asymmetric circular polarizer is obtained by placing a 45° rotated polarizer between two quarter-wave plates with their slow axes orthogonal to each other. Symmetric and asymmetric circular polarizers can also be implemented with stacked, high-contrast, subwavelength gratings. A compact and integrated realization of a symmetric circular polarizer is shown in Fig.4d.

In addition to transmissive structures, dielectric metasurfaces can also operate in reflection, with a target performance given by \mathbf{S}_{11} and \mathbf{S}_{22} , describing reflection from either side of the structure. For example, a metasurface realizing a reflective half-wave plate from one side and a reflective quarter-wave plate from the other is depicted in Fig.5. The reflective half-wave plate imparts a broadband 180° phase difference between orthogonal field components in reflection [28]. The reflection matrix of such a device is given by,

$$\mathbf{S}_{11}^d = \mathbf{rH} \equiv e^{j\phi} \begin{pmatrix} -1 & 0 \\ 0 & 1 \end{pmatrix}, \quad (27)$$

It rotates by 90° the polarization of an incident wave linearly polarized along $\hat{\mathbf{x}} \pm \hat{\mathbf{y}}$.

The reflective quarter-wave plate [89], imparts a 90° phase difference between orthogonal field components in

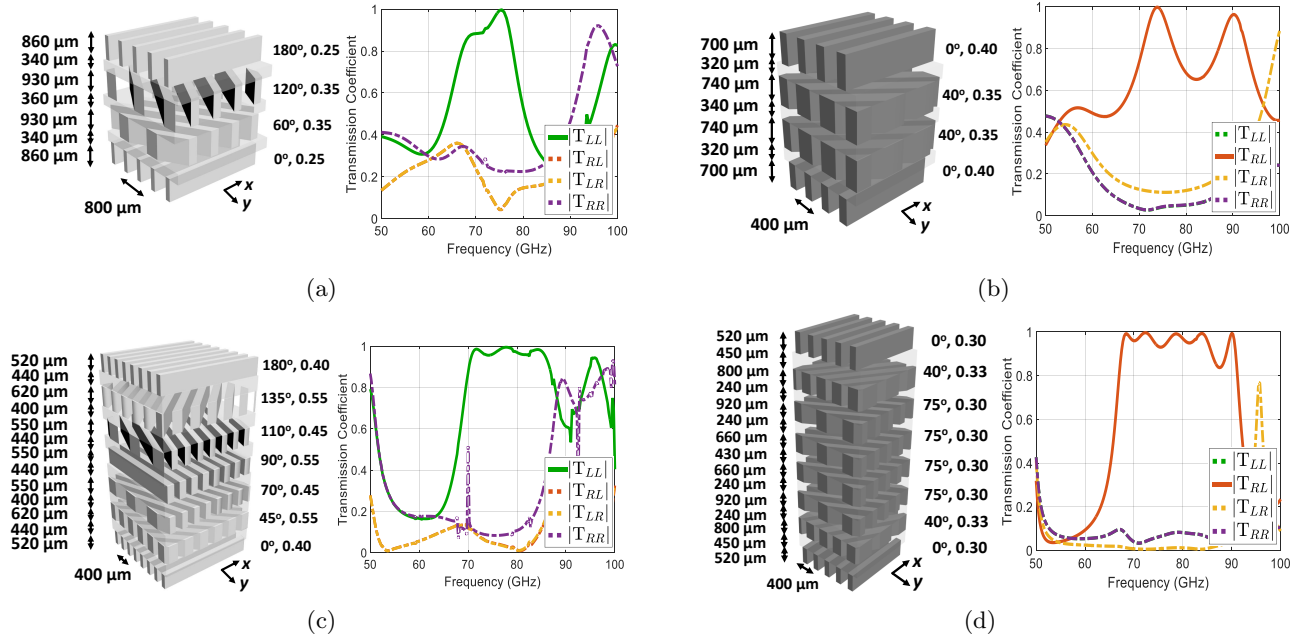


FIG. 6: Cascaded all-dielectric metasurfaces realizing a (a) narrowband symmetric circular polarizer, (b) narrowband asymmetric circular polarizer, (c) broadband symmetric circular polarizer, and (d) broadband asymmetric circular polarizer. The plots show that the bandwidth is improved with additional layers. The total thickness of the structures are (a) $1.15 \lambda_0$ (b) $0.96 \lambda_0$ (c) $1.62 \lambda_0$ (d) $2.02 \lambda_0$, where λ_0 is the wavelength at center frequency of 75 GHz.

reflection,

$$\mathbf{S}_{22}^d = \mathbf{r}\mathbf{Q} \equiv e^{j\phi} \begin{pmatrix} 1 & 0 \\ 0 & j \end{pmatrix}. \quad (28)$$

This results in the conversion of an incident wave, linearly polarized along $\hat{\mathbf{x}} \pm \hat{\mathbf{y}}$, to a circularly polarized reflected wave.

A. Broadband Polarization Conversion

The bandwidth of a multilayer dielectric metasurface can be improved with additional layers. It can be systematically increased by optimizing the cost function at multiple layer thicknesses. The electrical thickness of the layers can be used as a design variable to tailor the frequency response. Scaling the electrical thickness of all the layers is equivalent to shift in frequency, since the effective permittivity of a grating is independent of frequency when the grating period remains subwavelength across the operating bandwidth. Therefore, by scaling the electrical thicknesses of anisotropic gratings and isotropic spacers ($\varphi_i^{aniso}, \varphi_i^{iso}$) and minimizing the cost function at each thickness, one can control the spectral response. In design, the number of layers is gradually increased (1, 2, 3, . . .) and the cost function is minimized for each number of layers. Once the minimum of the cost function is found for a certain number of layers, it is compared to the convergence criterion given by Eq.(22) The design process is terminated when convergence criterion is

met: the cost function falls below a given value of ϵ . For example, a cascaded structure with 8 grating layers can have a broader bandwidth than is achievable with a 4 layer design (Fig.6). In order to obtain 10% fractional bandwidth, the cost function is optimized for electrical thicknesses,

$$\varphi_i^{aniso} = r \varphi_{i0}^{aniso}, \quad \varphi_i^{iso} = r \varphi_{i0}^{iso}, \quad (29)$$

where,

$$r \in [0.95 \ 1.05]. \quad (30)$$

The variables φ_0^{iso} and φ_0^{aniso} are the free-space electrical thicknesses of the isotropic spacer and the subwavelength grating at the center frequency. They can be related to physical thicknesses of the layers using,

$$\varphi_0^{aniso} = k_0 d_g, \quad \varphi_0^{iso} = k_0 d_s, \quad (31)$$

where k_0 is the free-space wavenumber corresponding to the center frequency. Variables d_g and d_s are the physical thicknesses of the grating and spacer layers.

The variable ϕ in the Jones matrices (Eqs.(20)-(28)) represents the total phase delay of the response. It is the phase difference between the incident and transmitted/reflected waves. It should be noted that variable ϕ is independently optimized at each scaled thickness to obtain the optimum performance.

The described technique can be followed to design polarization controlling metasurfaces of different bandwidths. Examples of broadband metasurfaces operating

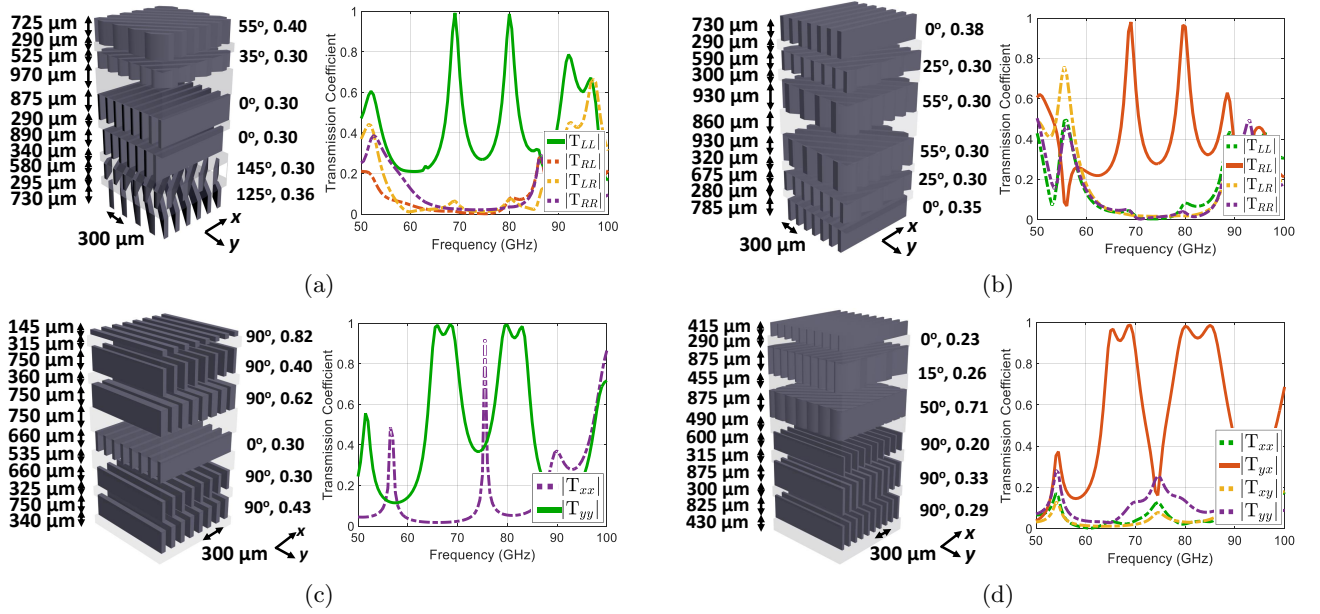


FIG. 7: Cascaded subwavelength grating metasurfaces realizing a (a) dual-band (70, 80 GHz) symmetric circular polarizer, (b) dual-band asymmetric circular polarizer, (c) dual-band symmetric linear polarizer, (d) dual-band asymmetric linear polarizer. The gratings and spacers are assumed to be silicon and the trenches air-filled.

at millimeter-wave frequencies are shown in Fig.6. For example, the symmetric circular polarizers, depicted in Fig.6a and Fig.6c, are designed assuming alumina [90–92] gratings, alumina spacers, and air-filled trenches,

$$\epsilon_g = \epsilon_s = 9.7, \quad \epsilon_t = 1. \quad (32)$$

Such devices can be manufactured through commercial ceramic stereolithography processes [91]. Similarly, the asymmetric circular polarizers, shown in Fig.6b and Fig.6d, are designed with Silicon [92, 93] gratings, Silicon spacers, and air-filled trenches,

$$\epsilon_g = \epsilon_s = 11.7, \quad \epsilon_t = 1. \quad (33)$$

High-resistivity silicon wafers can be patterned using Deep Reactive Ion Etching (DRIE) or dicing processes [94], and then stacked to build these structures.

B. Multiband Polarization Conversion

In addition to broadband frequency responses, the metasurfaces consisting of cascaded subwavelength gratings can be designed to operate across multiple frequency bands. Multiband structures are shown in Fig.7 consisting of silicon gratings and spacers (Eq.(33)). Dual-band symmetric and asymmetric circular polarizers are shown in Fig.7a and Fig.7b operating at 70 and 80 GHz. These dual-band metasurfaces have been designed by scaling the thickness of the layers at 75 GHz by the factors,

$$r_1 = \frac{70}{75}, \quad r_2 = \frac{80}{75}, \quad (34)$$

and then minimizing their associated cost function at the scaled thicknesses.

The dual-band symmetric and asymmetric x linear polarizers, operating over wider bandwidths, (Fig.7d) are designed by minimizing the cost function at thicknesses, scaled by,

$$r_1 = \frac{65}{75}, \quad r_2 = \frac{70}{75}, \quad r_3 = \frac{80}{75}, \quad r_4 = \frac{85}{75}. \quad (35)$$

Again, 75 GHz is the frequency at which the electrical thicknesses are converted to physical thicknesses using Eq.(31).

Triple-band and quad-band structures can also be designed using this same approach. For example, a triple-band response operating at 60, 75, and 80 GHz can be obtained by minimizing the associated cost function at thicknesses scaled by the factors,

$$r_1 = \frac{60}{75}, \quad r_2 = \frac{75}{75}, \quad r_3 = \frac{80}{75}. \quad (36)$$

Multiband metasurfaces can be designed to realize different loss-less reciprocal polarization transformations at arbitrary frequency bands using the outlined approach.

C. Multifunctional Polarization Conversion

In multifunctional polarization conversion, a range of polarization transformations is distributed over multiple frequency bands. Multifunctional metasurfaces are shown in Fig.8. In Fig.8a, a dual-band, dual-function metasurface that functions as a left-handed symmetric

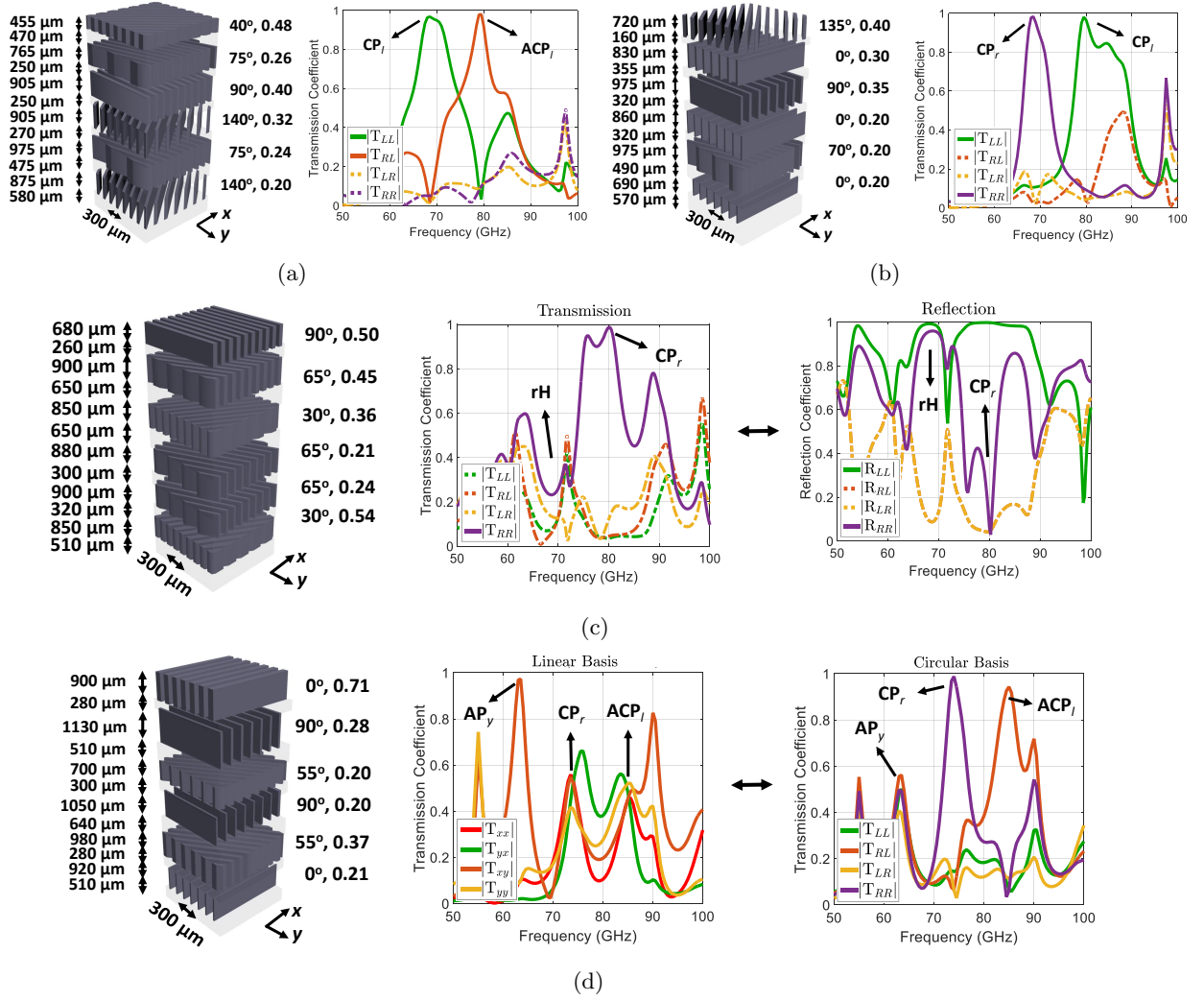


FIG. 8: Cascaded all-dielectric metasurfaces realizing a (a) dual-function symmetric and asymmetric left-handed circular polarizers, (b) dual-function right-handed and left-handed symmetric circular polarizers, (c) dual-function reflective half-wave plate and right-handed symmetric circular polarizer, and (d) a triple-function asymmetric y linear polarizer (plot on the left in linear basis), right-handed symmetric circular polarizer, and left-handed asymmetric circular polarizer (plot on the right in circular basis).

circular polarizer for one band and a left-handed asymmetric circular polarizer at a higher band is shown. As before, we scale the electrical thicknesses of the component layers by the ratios of the operating frequencies. Therefore, the electrical thicknesses of the constitutive layers are scaled by a factor $r_1 = 70/75$ and $|\mathbf{S}_{21} - \text{CP}_l|$ is evaluated at the scaled thickness. Simultaneously, the electrical thicknesses are scaled by $r_2 = 80/75$ and $|\mathbf{S}_{21} - \text{ACP}_l|$ is computed. Then the cost function,

$$|\mathbf{S}_{21} - \text{CP}_l|_{r=r_1} + |\mathbf{S}_{21} - \text{ACP}_l|_{r=r_2} \quad (37)$$

is minimized to achieve a symmetric left-handed circular polarizer (CP_l) operating at 70 GHz and an asymmetric left-handed circular polarizer (ACP_l) operating at 80 GHz.

The dual-function metasurface, shown in Fig.8b, re-

alizes a right-handed symmetric circular polarizer at a lower band (70 GHz) and a left-handed symmetric circular polarizer at an upper band (80 GHz). It is designed by scaling the thicknesses by the factors $r_1 = 70/75$ and $r_2 = 80/75$, and evaluating $|\mathbf{S}_{21} - \text{CP}_r|$ and $|\mathbf{S}_{21} - \text{CP}_l|$ at the respective thicknesses, and minimizing the cost function,

$$|\mathbf{S}_{21} - \text{CP}_r|_{r=r_1} + |\mathbf{S}_{21} - \text{CP}_l|_{r=r_2}. \quad (38)$$

Multifunctional responses can operate both in reflection and transmission. A metasurface realizing a reflective half-wave plate and a transmissive right-handed circular polarizer (Fig.8c) is obtained by scaling the electrical thicknesses by $r_1 = 70/75$ and $r_2 = 80/75$, then minimizing $|\mathbf{S}_{11} - \text{rH}|$ and $|\mathbf{S}_{21} - \text{CP}_r|$ at each thickness, respectively.

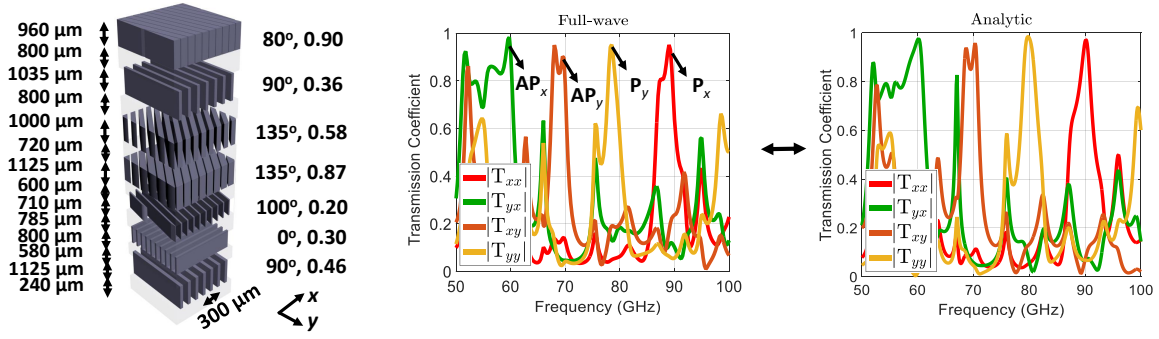


FIG. 9: Comparison between full-wave simulation and analytical computation. The quad-functional metasurface is designed to perform symmetric and asymmetric x and y linear polarizers at 60, 70, 80, and 90 GHz.

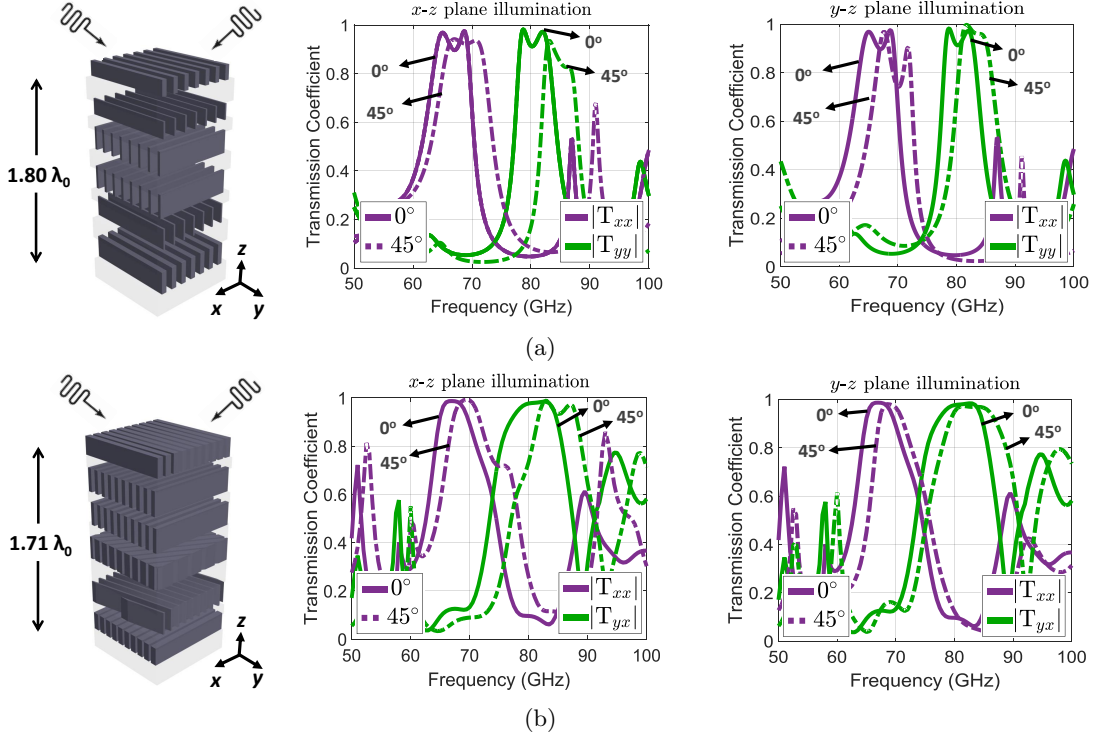


FIG. 10: Dual-function metasurfaces, realizing (a) x and y symmetric linear polarizers, (b) symmetric and asymmetric x linear polarizers at lower and upper bands. the cascaded metasurfaces show a robust performance under different illumination angles. The wave impinges the metasurfaces in the x - z ($\phi = 0^\circ$) and y - z ($\phi = 90^\circ$) planes at $\theta = 45^\circ$.

Multifunctional metasurfaces can also realize linear and circular polarizers at different bands. Fig.8d, shows a triple-function response realizing an asymmetric y linear polarizer, a right-handed circular polarizer, and a left-handed asymmetric circular polarizer at 65, 75, and 85 GHz bands, respectively. In Fig.8d, the performance is depicted in both linear and circular basis.

A multifunctional structure is shown in Fig.9 that includes x and y linear, symmetric and asymmetric polarizer responses over four frequency bands. The numerically computed and analytical frequency responses of the cascaded structure are shown. The analytical response is computed for normally incident waves by

scaling (Eq.(29)) the electrical thicknesses over the frequency range of interest and calculating the S-matrix from Eq.(17). In Fig.9, the analytic performance of the metasurface, from 50-100 GHz, is computed by sweeping r over,

$$r \in [50/75, 100/75], \quad (39)$$

and then computing the transmission matrices at the scaled thicknesses. As shown in Fig.9, there is close agreement between the full-wave and analytical performances when the gratings are deeply subwavelength. Discrepancies appear as the period of the grating layers becomes larger and the gratings can no longer be approx-

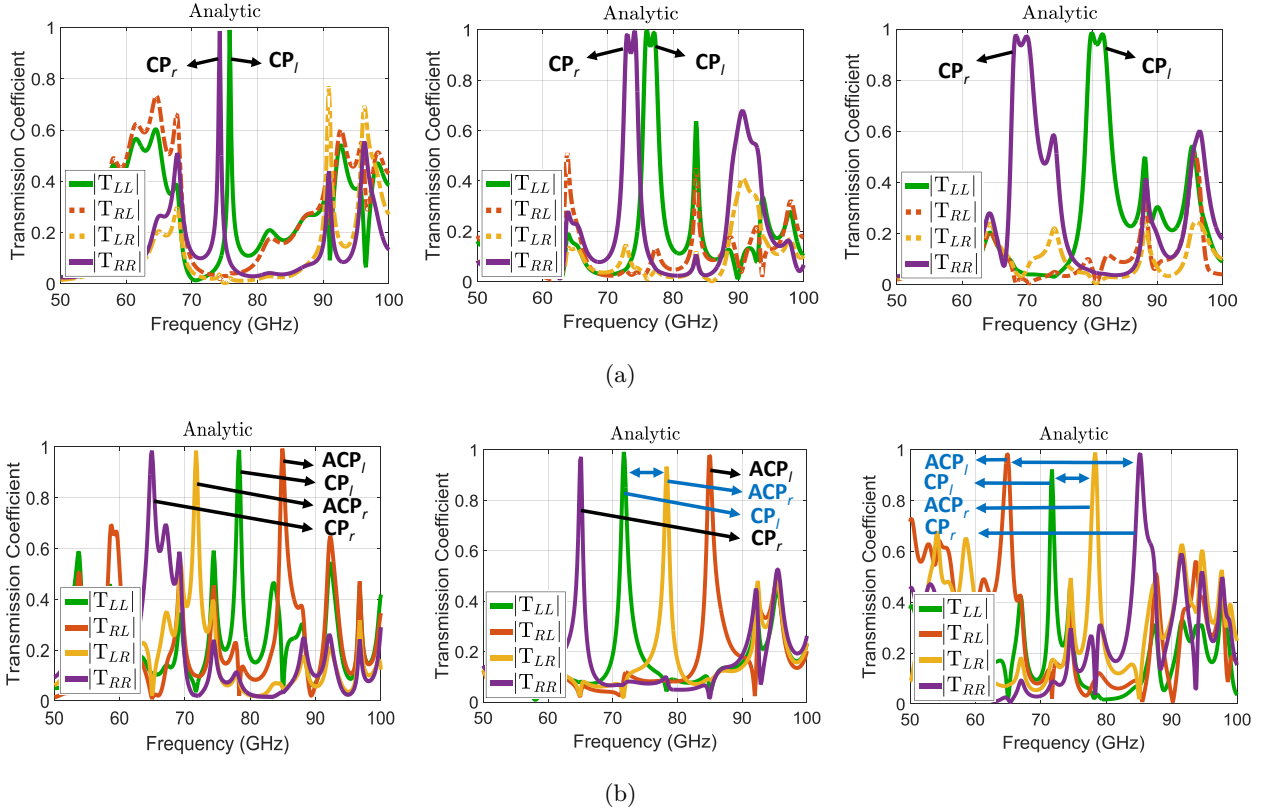


FIG. 11: (a) Dual-function responses at arbitrary frequency bands with different bandwidths. The performance of the dual-function left-handed and right-handed symmetric circular polarizer is changed from a right-handed to a left-handed symmetric circular polarizer over a 2% change in frequency. (b) Quad-functional metasurface that realizes symmetric and asymmetric, right-handed and left-handed circular polarizers in different orders.

imated as a uniaxial slab. The high aspect ratio of the gratings used can be mitigated by increasing its periodicity and using a more exact model for the effective permittivities and electrical thicknesses of the gratings as a uniaxial slab [82–84]. This would require a more computationally intensive optimization process.

Metasurfaces composed of cascaded gratings have a robust angular performance despite their wavelength-sized thickness. In Fig.10a, a dual-function symmetric x and y linear polarizer is studied under different excitation angles. Its frequency response is robust for angles of incidence up to $\theta = 45^\circ$ in x - z and y - z planes. Similarly, the response of the symmetric and asymmetric x linear polarizer is depicted in Fig.10b. It should be noted that the angular performance shown in Fig.10 was computed using full-wave simulation. Analytical techniques can also be used to find the angular performance [95], but it is beyond the scope of this work.

Fig.11a shows that a dual-function right-handed and left-handed symmetric circular polarizer can be designed with a 2% separation between frequencies. Fig.11b shows that four different scattering functions can be arranged in an arbitrary order with respect to frequency. In Fig.11, analytical frequency responses are presented. The full-

wave simulations are not shown given the close agreement between full-wave simulation and analytical computation (Fig.9) when the grating layers are deeply subwavelength. The corresponding structures are also not presented considering that similar topologies are used. Symmetric and asymmetric, left-handed and right-handed circular polarizers are chosen, however, these findings are applicable to many other scattering performances.

V. CONCLUSION

In this work, cascaded all-dielectric metasurfaces are investigated. The metasurfaces consist of stacked, high-contrast, subwavelength gratings with varying crystal axes. A systematic approach to their design is discussed. A variety of polarization transforming designs are reported. Multiband and multifunctional polarization control using such metasurfaces is also introduced. The reported structures and design approach will find application in the realization of compact, low-loss, broadband, multiband, and multifunctional polarization controlling and frequency filtering optical and quasi-optical devices. In future work, these structures will be experimentally

demonstrated using various fabrication processes.

VI. ACKNOWLEDGEMENT

This work was supported by Office of Naval Research (ONR) under Grant No.N00014-15-1-2390.

VII. REFERENCES

-
- [1] L. Wolff, Polarization vision: a new sensory approach to image understanding, *Image and Vision Computing*, vol. 15, no. 2, pp. 81-93, 1997.
- [2] A. Pierangelo, A. Benali, M. Antonelli, T. Novikova, P. Validire, B. Gayet and A. De Martino, Ex-vivo characterization of human colon cancer by Mueller polarimetric imaging, *Optics Express*, vol. 19, no. 2, p. 1582, 2011.
- [3] M. Brodsky, N. Frigo, M. Boroditsky and M. Tur, Polarization Mode Dispersion of Installed Fibers, *Journal of Lightwave Technology*, vol. 24, no. 12, pp. 4584-4599, 2006.
- [4] C. Pfeiffer and A. Grbic, Bianisotropic Metasurfaces for Optimal Polarization Control: Analysis and Synthesis, *Phys. Rev. Applied*, vol. 2, no. 4, 2014.
- [5] Z. Wei, Y. Cao, Y. Fan, X. Yu and H. Li, Broadband polarization transformation via enhanced asymmetric transmission through arrays of twisted complementary split-ring resonators, *Applied Physics Letters*, vol. 99, no. 22, p. 221907, 2011.
- [6] S. Momeni Hasan Abadi and N. Behdad, A broadband, circular-polarization selective surface, *Journal of Applied Physics*, vol. 119, no. 24, p. 244901, 2016.
- [7] A. Ericsson and D. Sjöberg, Design and Analysis of a Multilayer Meander Line Circular Polarization Selective Structure, *IEEE Transactions on Antennas and Propagation*, vol. 65, no. 8, pp. 4089-4101, 2017.
- [8] T. Niemi, A. Karilainen and S. Tretyakov, Synthesis of Polarization Transformers, *IEEE Transactions on Antennas and Propagation*, vol. 61, no. 6, pp. 3102-3111, 2013.
- [9] C. Pfeiffer, C. Zhang, V. Ray, L. Guo and A. Grbic, High Performance Bianisotropic Metasurfaces: Asymmetric Transmission of Light, *Physical Review Letters*, vol. 113, no. 2, 2014.
- [10] M. Khorasaninejad and F. Capasso, Metalenses: Versatile multifunctional photonic components, *Science*, vol. 358, no. 6367, p. eaam8100, 2017.
- [11] Z. Yang, R. Jiang, X. Zhuo, Y. Xie, J. Wang and H. Lin, Dielectric nanoresonators for light manipulation, *Physics Reports*, vol. 701, pp. 1-50, 2017.
- [12] S. Glybovski, S. Tretyakov, P. Belov, Y. Kivshar and C. Simovski, Metasurfaces: From microwaves to visible, *Physics Reports*, vol. 634, pp. 1-72, 2016.
- [13] S. Chang, X. Guo and X. Ni, Optical Metasurfaces: Progress and Applications, *Annual Review of Materials Research*, vol. 48, no. 1, 2016.
- [14] A. Petosa and A. Ittipiboon, Dielectric Resonator Antennas: A Historical Review and the Current State of the Art, *IEEE Antennas and Propagation Magazine*, vol. 52, no. 5, pp. 91-116, 2010.
- [15] Kwok Wa Leung, Eng Hock Lim and Xiao Sheng Fang, Dielectric Resonator Antennas: From the Basic to the Aesthetic, *Proceedings of the IEEE*, vol. 100, no. 7, pp. 2181-2193, 2012.
- [16] A. Krasnok, A. Miroshnichenko, P. Belov and Y. Kivshar, All-dielectric optical nanoantennas, *Optics Express*, vol. 20, no. 18, p. 20599, 2012.
- [17] L. Zou, W. Withayachumnankul, C. Shah, A. Mitchell, M. Bhaskaran, S. Sriram and C. Fumeaux, Dielectric resonator nanoantennas at visible frequencies, *Optics Express*, vol. 21, no. 1, p. 1344, 2013.
- [18] V. Vashistha, G. Vaidya, P. Gruszecki, A. Serebryannikov and M. Krawczyk, Polarization tunable all-dielectric color filters based on cross-shaped Si nanoantennas, *Scientific Reports*, vol. 7, no. 1, 2017.
- [19] F. Rodríguez-Fortuño, A. Espinosa-Soria and A. Martínez, Exploiting metamaterials, plasmonics and nanoantennas concepts in silicon photonics, *Journal of Optics*, vol. 18, no. 12, p. 123001, 2016.
- [20] C. Pfeiffer and A. Grbic, Metamaterial Huygens' Surfaces: Tailoring Wave Fronts with Reflectionless Sheets, *Physical Review Letters*, vol. 110, no. 19, 2013.
- [21] I. Staude, A. Miroshnichenko, M. Decker, N. Fofang, S. Liu, E. Gonzales, J. Dominguez, T. Luk, D. Neshev, I. Brener and Y. Kivshar, Tailoring Directional Scattering through Magnetic and Electric Resonances in Subwavelength Silicon Nanodisks, *ACS Nano*, vol. 7, no. 9, pp. 7824-7832, 2013.
- [22] S. Liu, A. Vaskin, S. Campione, O. Wolf, M. Sinclair, J. Reno, G. Keeler, I. Staude and I. Brener, Huygens' Metasurfaces Enabled by Magnetic Dipole Resonance Tuning in Split Dielectric Nanoresonators, *Nano Letters*, vol. 17, no. 7, pp. 4297-4303, 2017.
- [23] A. Arbabi, Y. Horie, M. Bagheri and A. Faraon, Dielectric metasurfaces for complete control of phase and polarization with subwavelength spatial resolution and high transmission, *Nature Nanotech*, vol. 10, no. 11, pp. 937-943, 2015.
- [24] M. Khorasaninejad, W. Chen, R. Devlin, J. Oh, A. Zhu and F. Capasso, Metalenses at visible wavelengths: Diffraction-limited focusing and subwavelength resolution imaging, *Science*, vol. 352, no. 6290, pp. 1190-1194, 2016.
- [25] J. Ginn, I. Brener, D. Peters, J. Wendt, J. Stevens, P. Hines, L. Basilio, L. Warne, J. Ihlefeld, P. Clem and M. Sinclair, Realizing Optical Magnetism from Dielectric Metamaterials, *Physical Review Letters*, vol. 108, no. 9, 2012.
- [26] Q. Zhao, J. Zhou, F. Zhang and D. Lippens, Mie resonance-based dielectric metamaterials, *Materials To-*

- day, vol. 12, no. 12, pp. 60-69, 2009.
- [27] P. Spinelli, M. Verschuuren and A. Polman, Broadband omnidirectional antireflection coating based on subwavelength surface Mie resonators, *Nature Communications*, vol. 3, p. 692, 2012.
- [28] Y. Yang, W. Wang, P. Moitra, I. Kravchenko, D. Briggs and J. Valentine, Dielectric Meta-Reflectarray for Broadband Linear Polarization Conversion and Optical Vortex Generation, *Nano Letters*, vol. 14, no. 3, pp. 1394-1399, 2014.
- [29] M. Kim and G. Eleftheriades, Highly efficient all-dielectric optical tensor impedance metasurfaces for chiral polarization control, *Optics Letters*, vol. 41, no. 20, p. 4831, 2016.
- [30] H. Jiang, W. Zhao and Y. Jiang, All-dielectric circular polarizer with nearly unit transmission efficiency based on cascaded tensor Huygens surface, *Optics Express*, vol. 24, no. 16, p. 17738, 2016.
- [31] B. Bai, K. Konishi, X. Meng, P. Karvinen, A. Lehmuskero, M. Kuwata-Gonokami, Y. Svirko and J. Turunen, Mechanism of the large polarization rotation effect in the all-dielectric artificially chiral nanogratings, *Optics Express*, vol. 17, no. 2, p. 688, 2009.
- [32] A. Miroshnichenko and Y. Kivshar, Fano Resonances in All-Dielectric Oligomers, *Nano Letters*, vol. 12, no. 12, pp. 6459-6463, 2012.
- [33] J. Zhang, K. MacDonald and N. Zheludev, Near-infrared trapped mode magnetic resonance in an all-dielectric metamaterial, *Opt. Express*, vol. 21, no. 22, p. 26721, 2013.
- [34] R. Bakker, D. Permyakov, Y. Yu, D. Markovich, R. Paniagua-Domínguez, L. Gonzaga, A. Samusev, Y. Kivshar, B. Luk'yanchuk and A. Kuznetsov, Magnetic and Electric Hotspots with Silicon Nanodimers, *Nano Letters*, vol. 15, no. 3, pp. 2137-2142, 2015.
- [35] S. Campione, S. Liu, L. Basilio, L. Warne, W. Langston, T. Luk, J. Wendt, J. Reno, G. Keeler, I. Brener and M. Sinclair, Broken Symmetry Dielectric Resonators for High Quality Factor Fano Metasurfaces, *ACS Photonics*, vol. 3, no. 12, pp. 2362-2367, 2016.
- [36] Y. Yang, I. Kravchenko, D. Briggs and J. Valentine, All-dielectric metasurface analogue of electromagnetically induced transparency, *Nature Communications*, vol. 5, p. 5753, 2014.
- [37] C. Wu, N. Arju, G. Kelp, J. Fan, J. Dominguez, E. Gonzales, E. Tutuc, I. Brener and G. Shvets, Spectrally selective chiral silicon metasurfaces based on infrared Fano resonances, *Nature Communications*, vol. 5, 2014.
- [38] M. Odit, P. Kapitanova, P. Belov, R. Alaee, C. Rockstuhl and Y. Kivshar, Experimental realisation of all-dielectric bianisotropic metasurfaces, *Applied Physics Letters*, vol. 108, no. 22, p. 221903, 2016.
- [39] C. Mateus, M. Huang, L. Chen, C. Chang-Hasnain and Y. Suzuki, Broad-Band Mirror (1.12–1.62 μm) Using a Subwavelength Grating, *IEEE Photonics Technology Letters*, vol. 16, no. 7, pp. 1676-1678, 2004.
- [40] N. Estakhri, V. Nader, M. Knight, A. Polman and A. Alù, Visible Light, Wide-Angle Graded Metasurface for Back Reflection, *ACS Photonics*, vol. 4, no. 2, pp. 228-235, 2017.
- [41] L. Piloizzi, D. Schiumarini, N. Tomassini and A. D'Andrea, Giant reflection band and anomalous negative transmission in a resonant dielectric grating slab: Application to a planar cavity, *Physical Review B*, vol. 86, no. 4, 2012.
- [42] F. Aieta, M. Kats, P. Genevet and F. Capasso, Multi-wavelength achromatic metasurfaces by dispersive phase compensation, *Science*, vol. 347, no. 6228, pp. 1342-1345, 2015.
- [43] M. Khorasaninejad, F. Aieta, P. Kanhaiya, M. Kats, P. Genevet, D. Rousso and F. Capasso, Achromatic Metasurface Lens at Telecommunication Wavelengths, *Nano Letters*, vol. 15, no. 8, pp. 5358-5362, 2015.
- [44] D. Fattal, J. Li, Z. Peng, M. Fiorentino and R. Beausoleil, Flat dielectric grating reflectors with focusing abilities, *Nature Photonics*, vol. 4, no. 7, pp. 466-470, 2010.
- [45] F. Lu, F. Sedgwick, V. Karagodsky, C. Chase and C. Chang-Hasnain, Planar high-numerical-aperture low-loss focusing reflectors and lenses using subwavelength high contrast gratings, *Optics Express*, vol. 18, no. 12, p. 12606, 2010.
- [46] R. Magnusson and S. Wang, New principle for optical filters, *Applied Physics Letters*, vol. 61, no. 9, pp. 1022-1024, 1992.
- [47] Y. Ko and R. Magnusson, Flat-top bandpass filters enabled by cascaded resonant gratings, *Optics Letters*, vol. 41, no. 20, p. 4704, 2016.
- [48] T. Gaylord and M. Moharam, Analysis and applications of optical diffraction by gratings, *Proceedings of the IEEE*, vol. 73, no. 5, pp. 894-937, 1985.
- [49] Z. Bomzon, V. Kleiner and E. Hasman, Pancharatnam–Berry phase in space-variant polarization-state manipulations with subwavelength gratings, *Optics Letters*, vol. 26, no. 18, p. 1424, 2001.
- [50] D. Lin, P. Fan, E. Hasman and M. Brongersma, Dielectric gradient metasurface optical elements, *Science*, vol. 345, no. 6194, pp. 298-302, 2014.
- [51] G. Nordin and P. Deguzman, Broadband form birefringent quarter-wave plate for the mid-infrared wavelength region, *Optics Express*, vol. 5, no. 8, p. 163, 1999.
- [52] H. Mosallaei and K. Sarabandi, Magneto-Dielectrics in Electromagnetics: Concept and Applications, *IEEE Transactions on Antennas and Propagation*, vol. 52, no. 6, pp. 1558-1567, 2004.
- [53] K. Ho, C. Chan, C. Soukoulis, R. Biswas and M. Sigalas, Photonic band gaps in three dimensions: New layer-by-layer periodic structures, *Solid State Communications*, vol. 89, no. 5, pp. 413-416, 1994.
- [54] A. Orlov, A. Krylova, S. Zhukovsky, V. Babicheva and P. Belov, Multiperiodicity in plasmonic multilayers: General description and diversity of topologies, *Physical Review A*, vol. 90, no. 1, 2014.
- [55] A. DaSilva, Y. Chang, T. Norris and A. MacDonald, Enhancement of photonic density of states in finite graphene multilayers, *Physical Review B*, vol. 88, no. 19, 2013.
- [56] D. Novitsky, V. Tuz, S. Prosvirnin, A. Lavrinenko and A. Novitsky, Transmission enhancement in loss-gain multilayers by resonant suppression of reflection, *Physical Review B*, vol. 96, no. 23, 2017.
- [57] C. Amra, M. Zerrad, F. Lemarchand, A. Lereu, A. Pasion, J. Zapien and M. Lequime, Energy density engineering via zero-admittance domains in all-dielectric stratified materials, *Physical Review A*, vol. 97, no. 2, 2018.
- [58] L. Sun, Z. Li, T. Luk, X. Yang and J. Gao, Nonlocal effective medium analysis in symmetric metal-dielectric multilayer metamaterials, *Physical Review B*, vol. 91, no. 19, 2015.

- [59] O. Shramkova and G. Tsironis, Propagation of electromagnetic waves in PT -symmetric hyperbolic structures, *Physical Review B*, vol. 94, no. 3, 2016.
- [60] K. Lee, J. Curzan, M. Shokooh-Saremi and R. Magnusson, Resonant wideband polarizer with single silicon layer, *Applied Physics Letters*, vol. 98, no. 21, p. 211112, 2011.
- [61] G. Zheng, J. Cong, L. Xu and W. Su, Compact polarizers with single layer high-index contrast gratings, *Infrared Physics & Technology*, vol. 67, pp. 408-412, 2014.
- [62] P. Deguzman and G. Nordin, Stacked subwavelength gratings as circular polarization filters, *Applied Optics*, vol. 40, no. 31, p. 5731, 2001.
- [63] P. Lalanne, S. Astilean, P. Chavel, E. Cambril and H. Launois, Design and fabrication of blazed binary diffractive elements with sampling periods smaller than the structural cutoff, *Journal of the Optical Society of America A*, vol. 16, no. 5, p. 1143, 1999.
- [64] B. Wilts, H. Whitney, B. Glover, U. Steiner and S. Vignolini, Natural Helicoidal Structures: Morphology, Self-assembly and Optical Properties, *Materials Today: Proceedings*, vol. 1, pp. 177-185, 2014.
- [65] S. Vignolini, P. Rudall, A. Rowland, A. Reed, E. Moyo-roud, R. Faden, J. Baumberg, B. Glover and U. Steiner, Pointillist structural color in Pollia fruit, *Proceedings of the National Academy of Sciences*, vol. 109, no. 39, pp. 15712-15715, 2012.
- [66] V. Sharma, M. Crne, J. Park and M. Srinivasarao, Structural Origin of Circularly Polarized Iridescence in Jeweled Beetles, *Science*, vol. 325, no. 5939, pp. 449-451, 2009.
- [67] J. D. Joannopoulos, R. D. Meade, and J. N. Winn, *Photonic Crystals: Molding the Flow of Light*. Princeton, NJ: Princeton Univ. Press, 1995.
- [68] Y. Cheng, R. Gong, Z. Cheng and Y. Nie, Perfect dual-band circular polarizer based on twisted split-ring structure asymmetric chiral metamaterial, *Applied Optics*, vol. 53, no. 25, p. 5763, 2014.
- [69] H. Xu, G. Wang, M. Qi, T. Cai and T. Cui, Compact dual-band circular polarizer using twisted Hilbert-shaped chiral metamaterial, *Optics Express*, vol. 21, no. 21, p. 24912, 2013.
- [70] M. Li, Q. Zhang, F. Qin, Z. Liu, Y. Piao, Y. Wang and J. Xiao, Microwave linear polarization rotator in a bilayered chiral metasurface based on strong asymmetric transmission, *Journal of Optics*, vol. 19, no. 7, p. 075101, 2017.
- [71] B. Lin, B. Wang, W. Meng, X. Da, W. Li, Y. Fang and Z. Zhu, Dual-band high-efficiency polarization converter using an anisotropic metasurface, *Journal of Applied Physics*, vol. 119, no. 18, p. 183103, 2016.
- [72] J. Shi, H. Ma, W. Jiang and T. Cui, Multiband stereometamaterial-based polarization spectral filter, *Physical Review B*, vol. 86, no. 3, 2012.
- [73] M. Kim and G. Eleftheriades, Design and Demonstration of Impedance-matched Dual-band Chiral Metasurfaces, *Scientific Reports*, vol. 8, no. 1, 2018.
- [74] J. Shi, X. Liu, S. Yu, T. Lv, Z. Zhu, H. Feng Ma and T. Jun Cui, Dual-band asymmetric transmission of linear polarization in bilayered chiral metamaterial, *Applied Physics Letters*, vol. 102, no. 19, p. 191905, 2013.
- [75] B. Lin, J. Guo, P. Chu, W. Huo, Z. Xing, B. Huang and L. Wu, Multiple-Band Linear-Polarization Conversion and Circular Polarization in Reflection Mode Using a Symmetric Anisotropic Metasurface, *Physical Review Applied*, vol. 9, no. 2, 2018.
- [76] A. Elsakka, V. Asadchy, I. Faniayeu, S. Tsvetkova and S. Tretyakov, Multifunctional Cascaded Metamaterials: Integrated Transmitarrays, *IEEE Transactions on Antennas and Propagation*, vol. 64, no. 10, pp. 4266-4276, 2016.
- [77] Z. Zhang, D. Wen, C. Zhang, M. Chen, W. Wang, S. Chen and X. Chen, Multifunctional Light Sword Metasurface Lens, *ACS Photonics*, 2018.
- [78] R. Hall, R. Mittra and K. Mitzner, Analysis of multilayered periodic structures using generalized scattering matrix theory, *IEEE Transactions on Antennas and Propagation*, vol. 36, no. 4, pp. 511-517, 1988.
- [79] A. Ranjbar and A. Grbic, Analysis and synthesis of cascaded metasurfaces using wave matrices, *Physical Review B*, vol. 95, no. 20, 2017.
- [80] A. Ranjbar and A. Grbic, All-dielectric Bianisotropic metasurfaces, in *Proceedings of the 2017 IEEE International Symposium on Antennas and Propagation USNC/URSI National Radio Science Meeting*, pp. 1719-1720.
- [81] Yariv, A. and P. Yeh, *Optical Waves in Crystals*, Wiley, New York, 1984.
- [82] P. Lalanne and D. Lemerrier-Lalanne, On the effective medium theory of subwavelength periodic structures, *Journal of Modern Optics*, vol. 43, no. 10, pp. 2063-2086, 1996.
- [83] P. Lalanne and D. Lemerrier-Lalanne, Depth dependence of the effective properties of subwavelength gratings, *Journal of the Optical Society of America A*, vol. 14, no. 2, p. 450, 1997.
- [84] V. Popov, A. Lavrinenko and A. Novitsky, Operator approach to effective medium theory to overcome a breakdown of Maxwell Garnett approximation, *Physical Review B*, vol. 94, no. 8, 2016.
- [85] P. Lalanne and J. Hugonin, High-order effective-medium theory of subwavelength gratings in classical mounting: application to volume holograms, *Journal of the Optical Society of America A*, vol. 15, no. 7, p. 1843, 1998.
- [86] H. Kikuta, Y. Ohira, H. Kubo and K. Iwata, Effective medium theory of two-dimensional subwavelength gratings in the non-quasi-static limit, *Journal of the Optical Society of America A*, vol. 15, no. 6, p. 1577, 1998.
- [87] A. Askarpour, Y. Zhao and A. Alù, Wave propagation in twisted metamaterials, *Phys. Rev. B*, vol. 90, no. 5, 2014.
- [88] J. Roy and L. Shafai, Reciprocal circular-polarization-selective surface, *IEEE Antennas and Propagation Magazine*, vol. 38, no. 6, pp. 18-33, 1996.
- [89] A. Pors and S. Bozhevolnyi, Efficient and broadband quarter-wave plates by gap-plasmon resonators, *Optics Express*, vol. 21, no. 3, p. 2942, 2013.
- [90] M. Afsar, Dielectric Measurements of Millimeter-Wave Materials, *IEEE Transactions on Microwave Theory and Techniques*, vol. 32, no. 12, pp. 1598-1609, 1984.
- [91] K. Brakora, J. Halloran and K. Sarabandi, Design of 3-D Monolithic MMW Antennas Using Ceramic Stereolithography, *IEEE Transactions on Antennas and Propagation*, vol. 55, no. 3, pp. 790-797, 2007.
- [92] M. Afsar and K. Button, Precise Millimeter-Wave Measurements of Complex Refractive Index, Complex Dielectric Permittivity and Loss Tangent of GaAs, Si, SiO₂, Al₂O₃, BeO, Macor, and Glass, *IEEE Transactions on Microwave Theory and Techniques*, vol. 31, no. 2, pp.

- 217-223, 1983.
- [93] M. Afsar and H. Chi, Millimeter wave complex refractive index, complex dielectric permittivity and loss tangent of extra high purity and compensated silicon, [International Journal of Infrared and Millimeter Waves](#), vol. 15, no. 7, pp. 1181-1188, 1994.
- [94] R. Datta, C. Munson, M. Niemack, J. McMahon, J. Britton, E. Wollack, J. Beall, M. Devlin, J. Fowler, P. Gallardo, J. Hubmayr, K. Irwin, L. Newburgh, J. Nibarger, L. Page, M. Quijada, B. Schmitt, S. Staggs, R. Thornton and L. Zhang, Large-aperture wide-bandwidth antireflection-coated silicon lenses for millimeter wavelengths, [Applied Optics](#), vol. 52, no. 36, p. 8747, 2013.
- [95] E. Glytsis and T. Gaylord, Rigorous three-dimensional coupled-wave diffraction analysis of single and cascaded anisotropic gratings, [Journal of the Optical Society of America A](#), vol. 4, no. 11, p. 2061, 1987.